ARTICLE

OPEN

Check for updates

Surface-wave instability without inertia in shear-thickening suspensions

Baptiste Darbois Texier[1], Henri Lhuissier[1], Yoël Forterre [1] & Bloen Metzger[1✉]

Recent simulations and experiments have shown that shear-thickening of dense particle suspensions corresponds to a frictional transition. Based on this understanding, non-monotonic rheological laws have been proposed and successfully tested in rheometers. These recent advances offer a unique opportunity for moving beyond rheometry and tackling quantitatively hydrodynamic flows of shear-thickening suspensions. Here, we investigate the flow of a shear-thickening suspension down an inclined plane and show that, at large volume fractions, surface kinematic waves can spontaneously emerge. Curiously, the instability develops at low Reynolds numbers, and therefore does not fit into the classical framework of Kapitza or 'roll-waves' instabilities based on inertia. We show that this instability, that we call 'Oobleck waves', arises from the sole coupling between the non-monotonic (S-shape) rheological laws of shear-thickening suspensions and the flow free surface.

[1] Aix-Marseille University, CNRS, IUSTI, Marseille 13453, France. ✉email: bloen.metzger@univ-amu.fr

How microscopic interactions affect the macroscopic flow behavior of complex fluids is at the core of soft matter physics. Recently, it has been shown that shear-thickening in dense particulate suspensions corresponds to a frictional transition at the microscopic scale; when the imposed shear stress exceeds the inter-particle short-range repulsive force, the grain contact interaction transits from frictionless to frictional[1–8]. During this transition, the proliferation of frictional contacts can be so massive that it triggers a remarkable macroscopic rheological response: the rate of shear of the suspension decreases when the imposed shear stress is increased. As a result, highly concentrated shear-thickening suspensions have peculiar S-shape rheological laws[9,10], which have been rationalized by a frictional transition model[3,11,12]. So far, the consequences of the frictional transition and its associated S-shape rheology have been essentially investigated in rheometers, where instabilities, shear bands and spatiotemporal patterns have been documented[11,13–15]. By contrast, very little is known about the behavior of shear-thickening suspensions in real hydrodynamic flow configurations beyond rheometry, in spite of the numerous applications[16–18].

An archetypal case, which is widely encountered in industrial and geophysical applications, is the incline plane flow configuration. As previously reported[19] and illustrated in Fig. 1a (see also Supplementary movie 2), when a thin layer of shear-thickening suspension flows down an inclined plane, surface waves of wavelengths much larger than the thickness can develop spontaneously and grow as they propagate downstream. This longwave free-surface instability may seem reminiscent of the Kapitza instability observed when a thin liquid film flows down a slope[20,21], or more generally of the so called "roll waves" instability observed from turbulent flows in open channels[22–24], to avalanches of complex fluids like mud[25,26] or granular media[27]. These latter two instabilities rely on the same primary mechanism: the amplification of kinematic surface waves at high velocity owing to inertial effects[28]. For a Newtonian liquid in the laminar regime, the destabilization occurs only when the Reynolds number of the flow, $Re = \rho u_0 h_0/\eta$, where ρ is the fluid density, u_0 its mean velocity, h_0 the flow thickness and η the fluid

viscosity, exceeds the Kapitza threshold, $Re_K = 5/(6 \tan \theta)$, which is typically much larger than 1 for a small tilting angle θ of the incline[29–31]. By contrast, the growth of surface waves observed in Fig. 1a for a dense shear-thickening suspension occurs at a Reynolds number of only ≈ 1, i.e., far below the Kapitza threshold $Re_K \approx 5$ predicted for $\theta = 10°$ (see also ref. [19]). This suggests that a different instability mechanism is at play for dense shear-thickening suspensions, yet its origin remains an open question.

Here, we investigate the origin of this instability by studying the flow of a shear-thickening suspension down an inclined plane over a wide range of volume fractions and flow rates. We confirm that this instability is not inertial and fundamentally different than the classical Kapitza or Roll waves instabilities. We provide experimental evidence together with a theoretical explanation, which show that this destabilization arises from the coupling between the flow free surface and the non-monotonic (S-shape) rheological laws of shear-thickening suspensions.

Results and discussion
Evidence of an instability distinct from the classical Kapitza or roll waves instabilities. We perform experiments with shear-thickening aqueous suspensions of commercial native cornstarch (Maisita®, http://www.agrana.com). We vary the particle volume fraction over a wide range ($0.30 < \phi < 0.48$) and characterize the onset of stability (the value of ϕ refers to the dry volume of cornstarch computed from its dry weight and density, $1550 \ kg \ m^{-3}$). We use a 1 m long and 10 cm wide inclined plane covered with a diamond lapping film (663-3M with roughnesses of $\sim 45 \ \mu m$) to insure rough boundary conditions. The suspension is released from a reservoir at the top of the plane through a gate with an adjustable aperture (Fig. 1b). A scale, placed at the bottom end of the incline (not shown in the schematic), provides the instantaneous flow rate q of the suspension. To probe the stability of this free-surface flow for moderate volume fractions $\phi \leq 0.4$, the gate is mounted on a translating stage imposing a small sinusoidal modulation of its aperture (3 Hz, $\pm 100 \ \mu m$). At large volume fractions however ($\phi \gtrsim 0.4$), no forcing is required because the flow is so unstable that it is dominated by noise amplification of its most unstable mode. Two
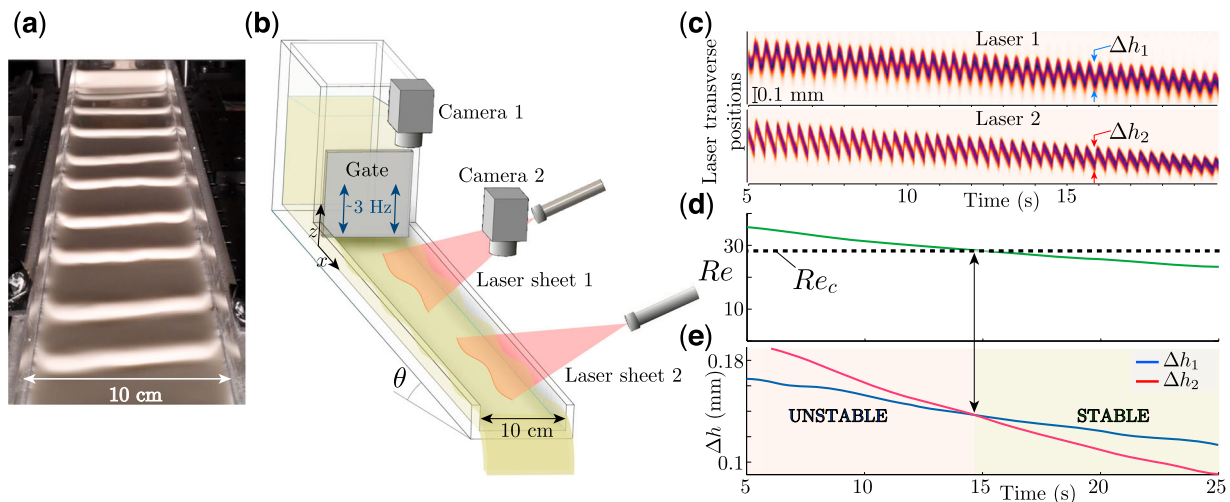

Fig. 1 Experimental characterization of the instability onset. a Non-inertial surface waves emerging spontaneously when a concentrated suspension of cornstarch particles flows down an incline (volume fraction $\phi = 0.45$, inclination angle $\theta = 10°$ and normalized flow Reynold number $Re/Re_K \approx 0.2$). **b** Sketch of the experimental setup. We use the progressive drainage of the reservoir to quasi-steadily vary the flow rate. The instability onset is determined by measuring the wave amplitudes both at the top and at the bottom of the incline with two laser sheets and cameras. For $\phi \leq 0.4$, an oscillation of the gate is added to impose a controlled perturbation. **c** Spatiotemporal plots of the laser sheet transverse-position versus time, indicating the vertical oscillations (blue and red arrows) of the free surface, at the top and at the bottom of the incline ($\phi = 0.33$, $\theta = 2°$, $Re \approx 37$). **d** Reynolds number of the flow, Re, and **e** amplitude of the perturbation at the top, Δh_1, and at the bottom, Δh_2, during the drainage of the suspension reservoir ($\phi = 0.36$, $\theta = 3°$). The instability onset ($\Delta h_1 = \Delta h_2$) is given by $Re_c \approx 28$ (black-dashed-line).

low-incident laser sheets and two cameras are used to measure the mean film thickness $h_0 \sim 2-10$ mm, and the crest-to-crest amplitude of the waves upstream and downstream of the incline (Fig. 1c). The calibration of the laser sheet projections on the film surface yields a local measurement of h_0 with a precision of 10 μm.

We use a protocol designed to characterize the instability onset with a single experiment for each volume fraction ϕ and inclination θ. The flow rate is varied quasi-steadily, either using the progressive drainage of the reservoir (decreasing flow rate) or by slowly increasing the gate aperture (increasing flow rate). At each instant, an effective Reynolds number of the flow is computed from the instantaneous flow rate q and from the mean film thickness h_0 using the relation $Re = 3q^2/(gh_0^3 \sin \theta)$, where g is the gravitational acceleration. Note that the flow rate is varied sufficiently slowly that at each instant, the flow rate is constant along the incline. With such a definition based on mean quantities only, the Reynolds number can be applied to any rheology and is directly related to the Froude number $F = u_0^2/(gh_0 \cos \theta)$ commonly used to described roll waves[24] by $Re = 3F/\tan\theta$, where $u_0 = q/h_0$ is the mean flow velocity. Re also reduces to the standard expression $Re = \rho u_0 h_0/\eta$ for a Newtonian fluid of viscosity η and density ρ in the laminar regime (Nusselt velocity profile). Figure 1d shows the concomitant evolution of Re and of the wave amplitude upstream (Δh_1) and downstream (Δh_2) the incline during the drainage of the reservoir, starting from an unstable situation where $\Delta h_2 > \Delta h_1$. The stability onset is precisely reached when $\Delta h_1 = \Delta h_2$, which provides us with the critical Reynolds number Re_c (dashed line in Fig. 1c), the critical flow thickness h_c, and the critical basal shear stress, $\tau_c = \rho g h_c \sin \theta$. We have verified that the same instability onset is obtained by carrying successive steady-state measurements at various constant flow rates. A new freshly prepared suspension of cornstarch is used for each measurement. Experiments are repeated four times for each volume fraction.

Figure 2a shows the critical Reynolds number Re_c, normalized by the Kapitza threshold for a Newtonian fluid, as a function of ϕ. For the lowest volume fraction investigated, $\phi = 0.30$, the stability threshold is close to Re_K (it is typically 50% above, owing to the finite forcing frequency and finite width of the plane[32,33]). As the volume fraction is increased, Re_c becomes increasingly larger relative to Re_K, reaching $\approx 5 Re_K$ at $\phi = 0.41$. This behavior is actually expected from Kapitza's inertial mechanism for a

medium that is continuously shear-thickening[34], like our cornstarch suspension over that range of volume fractions ($0.35 \lesssim \phi \lesssim 0.41$). More strikingly, for $\phi \gtrsim 0.41$ the relative critical Reynolds number drops drastically, down to two orders of magnitude below the Kapitza threshold at the largest volume fraction investigated ($\phi = 0.48$, for which $Re \approx 0.15$ and $F \approx 10^{-2}$). Clearly, in this domain, the flow destabilization can no longer be explained within the Kapitza framework since inertial effects are negligible. Note that inertia is also negligible at the particle scale, since the Stokes number, $St \sim (d/h_0)^2 Re$, where $d \sim 10$ μm is the particle size, is $\sim 10^5$ times smaller than Re. As shown in Fig. 2b, this qualitative change in the onset of instability around $\phi = 0.41$ is also observed in the evolution of the critical shear stress τ_c with ϕ. Similarly, the surface wave speed at the instability threshold changes significantly and abruptly. Its value c_c, normalized by the mean flow velocity u_0 drops from 3, which is Kapitza's prediction for a Newtonian layer in the long wavelength limit, to ~2 for volume fractions exceeding ≈ 0.41 (see Fig. 2c). These results confirm that above $\phi \approx 0.41$, a longwave free-surface instability, which is fundamentally distinct from the Kapitza instability, emerges. In the following, we call this instability, which to our knowledge as no equivalent in classical fluids, "Oobleck waves".

Oobleck waves arise from the S-shape rheology and kinematic wave propagation. To understand the origin of Oobleck waves, we characterize the rheology of the cornstarch suspension in a cylindrical-Couette rheometer (Fig. 3). We find that the volume fraction at which Oobleck waves appear ($\phi \approx 0.41$) corresponds precisely to ϕ_{DST}, the volume fraction at which the shear-thickening transition becomes discontinuous. Indeed, we analyze our rheological data along Wyart & Cates's model, which assumes that the effective viscosity of the suspension, $\eta(\phi, \tau) = \eta_s (\phi_J(\tau) - \phi)^{-2}$, diverges at a critical volume fraction, ϕ_J, that depends on the applied shear stress, τ, according to $\phi_J(\tau) = \phi_0(1 - e^{-\tau^*/\tau}) + \phi_1 e^{-\tau^*/\tau}$, where ($\eta_s$, τ^*, ϕ_0, ϕ_1) are material constant. Here, η_s is a prefactor proportional to the solvent viscosity, τ^* is the short-range repulsive stress scale above which the frictional transition occurs, which may be tuned by changing the particle roughness or surface chemistry, ϕ_0 (resp. ϕ_1) is the jamming volume fraction at which the suspension viscosity diverge at low (resp. large) stress, with ϕ_1 being dependent on the inter-particle friction coefficient[3]. By fitting our measurements
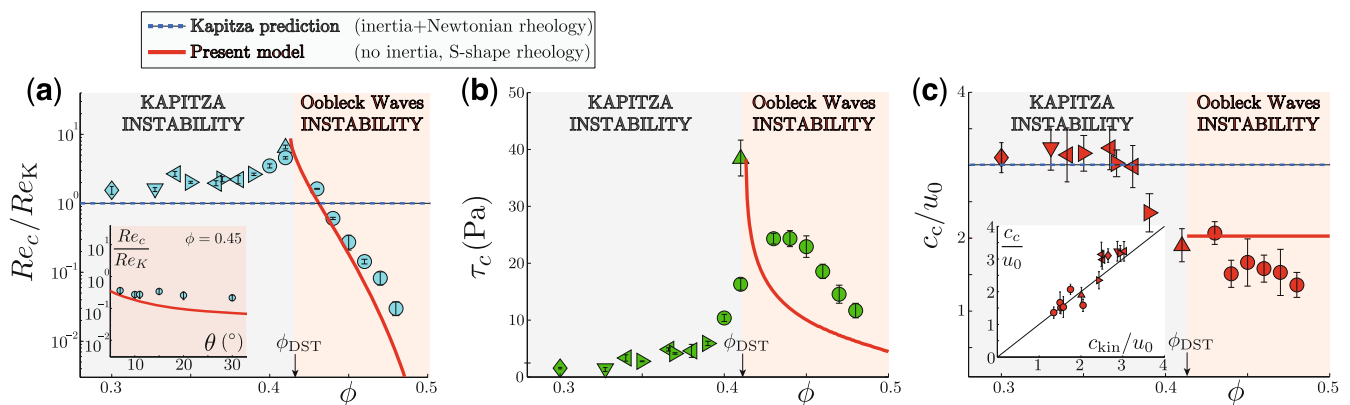

Fig. 2 Onset of instability. a Critical Reynolds number of the instability normalized by the Kapitza threshold Re_c/Re_k versus volume fraction ϕ. Inset: Re_c/Re_k versus inclination angle θ for $\phi = 0.45$. **b** Critical shear stress τ_c versus ϕ. **c** Normalized critical wave speed c_c/u_0 versus versus ϕ. Inset: c_c/u_0 versus speed of the kinematic waves c_{kin}/u_0, the black line shows that the waves propagate at the speed of the surface kinematic waves. Dashed-blue-line: Kapitza prediction (inertia+Newtonian fluid). Solid-red-line: prediction of the linear stability analysis ($A = d\tilde{\gamma}/d\tilde{\tau}_b|_{\bar{\tau}_b=1} = 0$) describing the coupling between the flow free-surface and the suspension shear-thickening rheology. Different symbols indicate different inclination angles θ: ◇ 2°, ▽ 3°, ▷ 6°, ◁ 9°, ○ 10°, △ 22°. The error bars indicate the standard deviation between experimental measurements. Different background colors highlight which instability emerges: Kapitza (gray) or Oobleck waves (red).
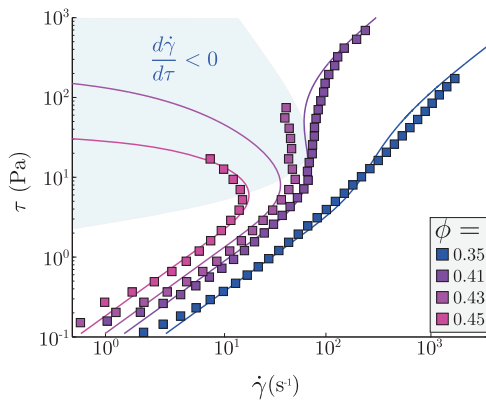
Fig. 3 Rheograms of the aqueous cornstarch suspension. Shear-stress τ versus shear rate $\dot{\gamma}$ for various volume fractions ϕ. Solid lines: fit by Wyart & Cates rheological laws setting the jamming volume fraction for frictionless and frictional particles to $\phi_0 = 0.52 \pm 0.005$ and $\phi_1 = 0.43 \pm 0.005$, respectively, the short-range repulsive stress scale above which the frictional transition occurs to $\tau^* = 12 \pm 2$ Pa and the prefactor to $\eta_s = 0.91 \pm 0.01$ mPa s. The rheograms are negatively sloped ($d\dot{\gamma}/d\tau < 0$) in the region highlighted in blue.

with this model, we find that the rheological curve (shear stress τ versus shear rate $\dot{\gamma}$) becomes S-shaped when $\phi \geq 0.41 \pm 0.005 = \phi_{DST}$ (see Fig. 3 and Methods for the fitting procedure). This suggests that negatively sloped portion in the rheological curve ($d\dot{\gamma}/d\tau < 0$) is a key ingredient of the instability. S-shaped flow curves, and more generally rheograms with a negatively sloped region, are known to produce unstable flow conditions[35,36]. Previous studies on shear-thickening suspensions have based their analysis on this feature to explain for instance the emergence of random fluctuations[37] reported initially by Boersma et al.[38], and the oscillations observed when an object moves in a shear-thickening fluid[39,40] or in rheometric configurations[15,41]. However, all these models require inertia to predict an instability. By contrast, here, the instability seems to be of a fundamentally different nature. First, it can occur at very low Reynolds and Froude numbers, for which inertial effects are negligible. Second, at the instability onset, the unstable mode propagates at the speed of the surface kinematic waves defined by $c_{kin} \equiv dq/dh_0$[28] (Fig. 2c inset). This indicates that the coupling between the flow and the free-surface deformation, which was not considered in previous studies, is essential to explain the emergence of Oobleck waves.

Oobleck waves instability mechanism. We now show how the negative slope in the rheology coupled with a gravity-driven free-surface flow can yield to an instability without invoking inertial effects. In the zero-Reynolds number limit, the force balance on a slice of suspension, as depicted in Fig. 4a, imposes that the basal stress, τ_b, is equal to the sum of the projected weight of the slice, $\rho g h \sin\theta$, where $h(x, t)$ is the local flow thickness, and of the longitudinal pressure gradient induced by the free-surface deflection. For wavelengths much larger than the flow thickness and the capillary length, the pressure profile perpendicular to the plane can be assumed to be hydrostatic $P(x, z, t) = \rho g \cos\theta(h(x, t) - z)$, where x is the flow direction and z the height within the flowing layer in the perpendicular direction[21]. The depth-averaged force balance is then given by

$$\tau_b = \rho g h \sin\theta - \rho g h \cos\theta \frac{\partial h}{\partial x}. \tag{1}$$

Let us now consider a perturbation of a base flow of constant thickness, as illustrated in Fig. 4b. A local increase of the flow thickness implies that $\partial h/\partial x$ becomes positive upstream of the

perturbation and negative downstream. To satisfy the force balance (1), the basal shear stress τ_b upstream must therefore decrease, whereas it must increase downstream. However, owing to the S-shape rheology of the suspension, when $d\dot{\gamma}/d\tau < 0$, a decrease (resp. increase) in τ_b implies a local increase (resp. decrease) of the flow rate $\dot{\gamma}$. Therefore, the shear rate increases upstream and decreases downstream, inducing a net inward mass flux underneath the bump and the amplification of the initial perturbation (red arrows in Fig. 4b).

Quantitative depth-averaged model without inertia. To go beyond this qualitative picture, we perform a linear stability analysis of a steady uniform flow of thickness h_0 and depth-averaged velocity u_0 using the Saint-Venant approximations (long wavelength limit[27,42]) and neglecting inertia (lubrication approximation[21]). The equations are written using the dimensionless variables $\tilde{h} = h/h_0$, $\tilde{x} = x/h_0$, $\tilde{u} = u/u_0$, $\tilde{t} = tu_0/h_0$, $\tilde{\tau}_b = \tau_b/\rho g h_0 \sin\theta$ and linearized by writing $\tilde{h} = 1 + h_1$, $\tilde{u} = 1 + u_1$ and $\tilde{\tau}_b = 1 + \tau_1$ with (h_1, u_1, $\tau_1 \ll 1$). Under these conditions, the mass conservation, $\partial_{\tilde{t}} h + \partial_{\tilde{x}}(hu) = 0$, and the force balance (1) become $\partial_{\tilde{t}} h_1 + \partial_{\tilde{x}} h_1 + \partial_{\tilde{x}} u_1 = 0$ and $\tau_1 = h_1 - \tan\theta^{-1}\partial_{\tilde{x}} h_1$, respectively. The linearization of the normalized shear-rate $\tilde{\dot{\gamma}}(\tilde{\tau}_b) \equiv \tilde{u}/\tilde{h}$, gives $A\tau_1 = u_1 - h_1$, where $A = d\tilde{\dot{\gamma}}/d\tilde{\tau}_b|_{\tilde{\tau}_b=1}$ is the slope of the rheological curve for the base state basal stress $\tau_b = \rho g h_0 \sin\theta$, obtained from the integration of the flow velocity profile (see Methods). Taking the spatial derivative of the force balance and substituting τ_1 and $\partial_{\tilde{x}} u_1$ using the rheology and mass balance, respectively, lead to a single partial differential equation for the free-surface perturbation h_1:

$$\frac{\partial h_1}{\partial \tilde{t}} + \tilde{c}\frac{\partial h_1}{\partial \tilde{x}} = \frac{A}{\tan\theta}\frac{\partial^2 h_1}{\partial \tilde{x}^2}, \tag{2}$$

where $\tilde{c} = c_{kin}/u_0 = 2 + A$ is the dimensionless speed of the kinematic waves[28]. Interestingly, the perturbation amplitude is found to follow a diffusion equation in the reference frame of the kinematic waves, with an effective "diffusion coefficient" $A/\tan\theta$. When $A < 0$, i.e., when the slope of the rheological law $u_0/h_0 = \dot{\gamma}(\tau_b)$ is negative, anti-diffusion occurs, which leads to an amplification of all perturbations, whereas for $A > 0$ the flow is stable. The onset of instability is thus given by $A = 0$. This criteria can be expressed in terms of a critical Reynolds number Re_c and a critical basal shear stress τ_c using the Wyart & Cates rheological laws (see Methods). Figures 2a, b show that, for $\phi \geq \phi_{DST}$, these predictions (red-solid lines) capture very well the value of the critical Reynolds Re_c and its dramatic drop over two decades when increasing ϕ, as well as the order of magnitude and the drop of the critical shear stress τ_c with ϕ. The decrease of the instability onset with increasing ϕ is a direct consequence of Wyart and Cates' rheological laws[3], where the DST onset stress also decreases with ϕ. Physically, it comes from the fact that, when approaching the maximal possible packing fraction ϕ_0, less and less frictional contacts are required to reach the DST region. The model also predicts a weak dependence of Re_c on the plane inclination angle, as observed experimentally (Fig. 2a inset). This overall agreement is all the more conclusive that it is rooted on physically based constitutive laws, of which the rheological parameters are measured independently, without further fitting. Another strong prediction of the model is that, at the instability onset ($A = 0$), the speed of the unstable mode is equal to the speed of the kinematic waves $c_c/u_0 = 2$. This prediction is fully consistent with the drop and value of the normalized wave speed observed experimentally for $\phi > \phi_{DST}$ (see Fig. 2c). These results conclusively show that surface waves can emerge from the coupling between a negatively sloped rheology and the flow free surface, without the need for inertial effects.
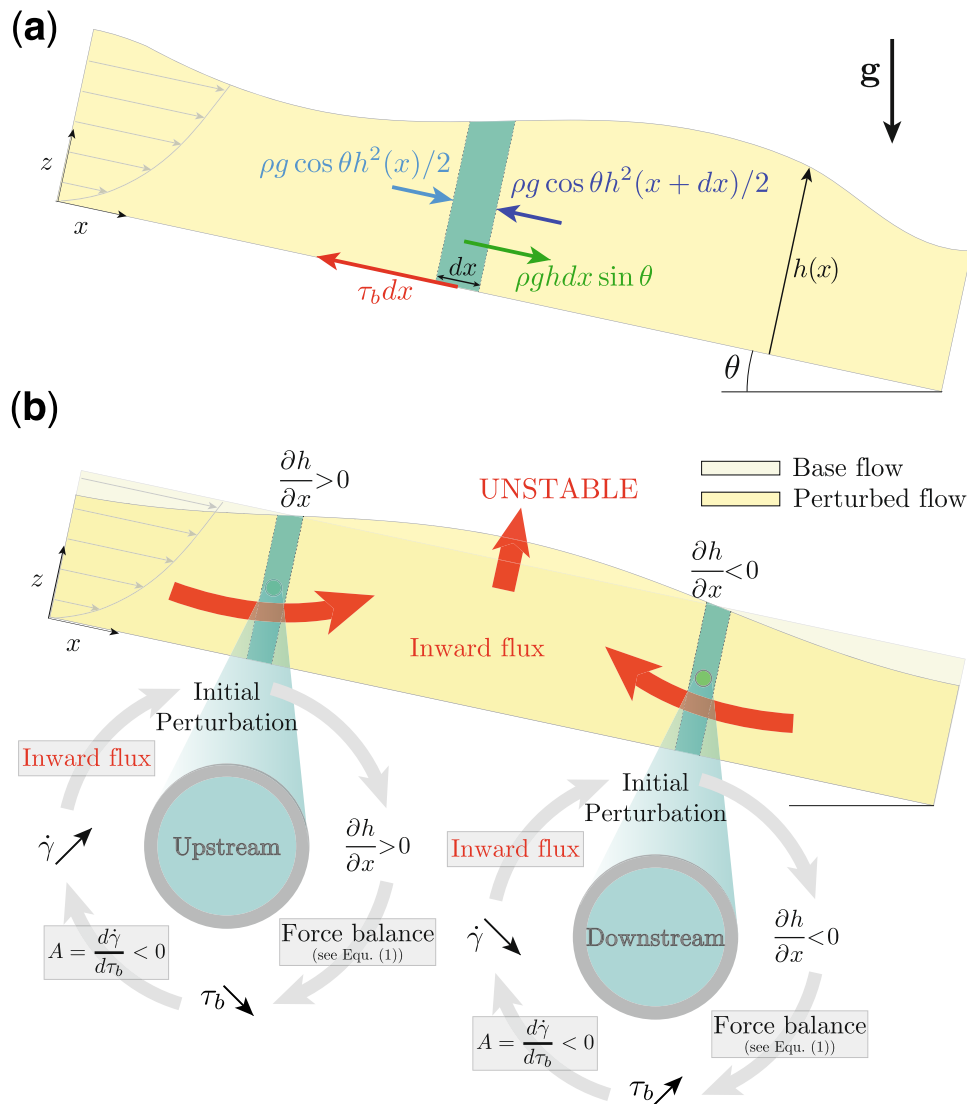
Fig. 4 Instability mechanism. a Depth-averaged forces acting along the flow x direction on a slice of suspension of width dx (shaded in blue): basal force $\tau_b dx$, projected weight of the slice $\rho g h dx \sin\theta$ and hydrostatic pressure $\rho g \cos\theta h^2(x)/2$, where τ_b is the basal shear stress, g is gravity, $h(x)$ is the flow thickness, θ is the plane inclination angle. **b** Positive feedback for a shear-thickening suspension with a S-shaped rheological curve: a local increase of the flow thickness h implies that $\partial h/\partial x$ is positive (resp. negative) upstream (resp. downstream) of the perturbation. Force balance (see Eq. (1)) then implies that the basal shear stress τ_b upstream (resp. downstream) must decrease (resp. increase). When the suspension rheogram is negatively sloped $(d\dot\gamma/d\tau<0)$, this yields a local increase (resp. decrease) of the flow rate $\dot\gamma$. The combination of these two feedback cycles (gray arrows) induces a net inward mass flux towards the bump (red arrows) that amplifies the initial perturbation (red vertical arrow).

The Oobleck waves instability mechanism highlighted in this study is not limited to shear-thickening suspensions and could be extended to any other complex fluids having a rheology with a negatively sloped region (e.g., granular materials and geomaterials exhibiting velocity-weakening rheology[43,44], concentrated polymers or surfactant solutions[35,36], liquid crystals[45], active self-propelled suspensions[46]). More generally, our analysis shows that gravity forces, which are usually stabilizing for gravity-driven free-surface flows, can become destabilizing in the presence of a non-monotonic rheology. Our result could thus be extended to other stabilizing forces such as capillary forces arising from the free-surface deformation. We thus anticipate that other interesting instabilities may be explained directly, or in the light of our study.

Finally, in a broader context, our study reveals that kinematic waves can be unstable in an overdamped medium, where inertia is negligible. These waves, which are observed in a wide range of situations (e.g., traffic and pedestrian flows[47], sediment transport[48], fluidized bed[49], surge, and floods[23]), result from mass conservation and a general relationship between a local flow rate and a local concentration[50,51] (e.g., number of vehicles or pedestrians on a road, solid packing fraction in a suspension, depth of the flow). However, in all these systems, their emergence from a uniform state requires an inertial lag between the flow rate and the concentration[28]. In our system, the situation is very different as these waves are unstable not from inertia, but from the intrinsic constitutive flow rule of the material. Whether this description of kinematic waves could be extended to more complex systems, such as crowds[47] or active self-propelled particles[46], are interesting topics to address in future studies.

Methods

Rheological data fitting procedure. Rheograms of the aqueous suspension of cornstarch are measured for various volume fractions in a narrow-gap cylindrical-
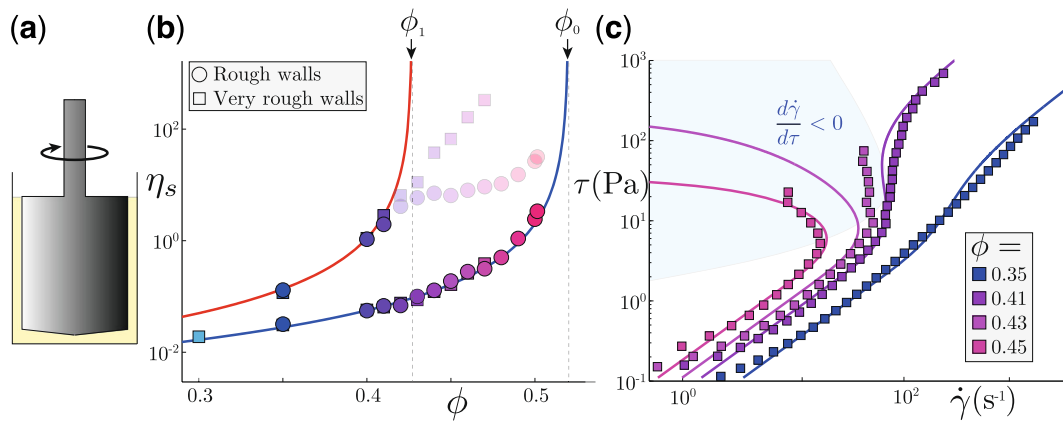
Fig. 5 Rheological data fitting procedure. a Cylindrical-Couette geometry used to characterize the rheology of the aqueous suspension of cornstarch (yellow). The gray area represents the cylinder rotating in the direction indicated by the black arrow. **b** Viscosity (Pa.s) below ($\tau \ll \tau^*$) and above ($\tau \gg \tau^*$) the shear-thickening transition versus ϕ. Blue-solid-line: frictionless branch, red-solid-line: frictional branch, black-dashed-lines: jamming volume fractions for the frictionless and frictional branches defining ϕ_0 and ϕ_1, respectively. Square and circle symbols correspond to measurements performed with different wall roughness. The data points made transparent are not used in the fitting procedure as for these points, the measurement depend on the wall roughness. **c** Shear stress τ versus shear rate $\dot{\gamma}$ measured at various volume fraction ϕ. Solid lines: Wyart & Cates rheological laws. The blue shaded area highlights the region where the rheograms are negatively sloped ($d\dot{\gamma}/d\tau < 0$).

Couette cell (Fig. 5a) using a rheometer (Anton Paar MCR 501). The height of the shear-cell (40 mm) is sufficiently large to neglect sedimentation effects of the particles during the measurement. Similarly to the procedure followed by Guy et al.[4], the viscosity below ($\tau \ll \tau^*$) and above ($\tau \gg \tau^*$) the shear-thickening transition are extracted and plotted versus ϕ (Fig. 5b). The low viscosity branch (frictionless branch) is first fitted with $\eta(\phi) = \eta_s(\phi_0 - \phi)^{-2}$, with η_s and ϕ_0 as fitting parameters. This yields $\eta_s = 0.91 \pm 0.01$ mPa.s and $\phi_0 = 0.52 \pm 0.005$. The large viscosity branch (frictional branch) is then fitted with $\eta(\phi) = \eta_s(\phi_1 - \phi)^{-2}$, using the previous estimation of η_s, and letting ϕ_1 as the only fitting parameter. Note that the rheograms are obtained using both very rough (square symbols) and rough walls (circle symbols), by covering the cell-walls with sand papers of different grades (roughnesses of ≈ 80 μm and ≈ 15 μm, respectively). The two measurements overlap, except in the frictional branch at high volume fraction (shaded symbols in Fig. 5b). For instance, the data from $\phi = 0.4$ and 0.41 are included in the fitting procedure, while 0.42 and 0.43 are not, because the first two points overlap, independently of the roughness of the boundaries, whereas for 0.42 and 0.43 systematic deviations are observed indicating slippage or other artefacts. All data points which are interpreted as biased measurements (transparent symbols) are discarded from the fitting procedure; this yields $\phi_1 = 0.43 \pm 0.005$. Once the values of η_s, ϕ_0 and ϕ_1 are set, we determine the value of τ^* by fitting the full rheograms $\tau(\dot{\gamma})$ with Wyart & Cates laws: $\tau = \eta_s(\phi_J(\tau) - \phi)^{-2}\dot{\gamma}$, with $\phi_J(\tau) = \phi_0(1 - e^{-\tau^*/\tau}) + \phi_1 e^{-\tau^*/\tau}$. The best fit, shown in Fig. 5c, is obtained for $\tau^* = 12 \pm 2$ Pa. The value of τ^* represents the critical shear stress required to overcome the inter-particle repulsive force and activate frictional contacts between particles. For an inter-particulate force f and a particle size d, the critical shear stress is expected to be of order f/d^2. The value we obtain (≈ 12 Pa) is consistent with the values already reported in the literature for cornstarch in water.

Computation of τ_c and Re_c. To compute the critical shear stress τ_c and the critical Reynold number Re_c from the instability criteria resulting from the linear stability analysis $A \equiv d\tilde{\dot{\gamma}}/d\tilde{\tau}_b|_{\tilde{\tau}_b=1} = 0$, we need to relate the shear rate $\dot{\gamma} \equiv u_0/h_0$, defined as the ratio of the depth-averaged flow velocity to the flow thickness, to the basal shear stress τ_b and the basal suspension viscosity $\eta(\tau_b)$.

For a steady uniform flow down an inclined plane of slope θ, the momentum equation applied to a surface layer of thickness $h_0 - z$ gives

$$\tau(z) = \rho g \sin\theta(h_0 - z) = \eta(z)\frac{d\hat{u}(z)}{dz}, \tag{3}$$

where the second equality uses the definition of viscosity, $\eta = \tau/(d\hat{u}/dz)$, and $\hat{u}(z)$ is the local velocity parallel to x. From the proportionality between τ and $h_0 - z$, the local velocity can be expressed as

$$\hat{u}(\tau) = \frac{1}{\rho g \sin\theta}\int_\tau^{\tau_b}\frac{\tau''}{\eta(\tau'')}d\tau''. \tag{4}$$

Using the definition of the depth-averaged flow velocity, $u_0 = \int_0^{\tau_b}\hat{u}(\tau')\,d\tau'/\tau_b$, we obtain the expression of the depth-averaged shear rate

$$\dot{\gamma} = \frac{\tau_b}{3\eta(\tau_b)}\mathcal{G}(\tau_b), \tag{5}$$

where

$$\mathcal{G}(\tau) = \frac{3\eta(\tau)}{\tau^3}\int_0^\tau\int_{\tau'}^\tau\frac{\tau''}{\eta(\tau'')}d\tau''d\tau', \tag{6}$$

embeds the shear-thickening of the suspension. By definition, $\mathcal{G} = 1$ for a Newtonian fluid.

From (5) and (6) we obtain

$$A \equiv \frac{d\tilde{\dot{\gamma}}}{d\tilde{\tau}_b}|_{\tilde{\tau}_b=1} = \frac{\tau_b}{\dot{\gamma}}\frac{d\dot{\gamma}}{d\tau_b}|_{\tau_b=\rho g \sin\theta h_0} = \frac{3}{\mathcal{G}(\tau_b)} - 2, \tag{7}$$

where we have used $\frac{d}{d\tau}(\int_0^\tau\int_{\tau'}^\tau\frac{\tau''}{\eta(\tau'')}d\tau''d\tau') = \tau^2/\eta(\tau)$. Note that in (7), the basal stress τ_b, the shear rate $\dot{\gamma}$ and the derivative are taken at the base state, i.e., for $\dot{\gamma} = u_0/h_0$ and $\tau_b = \rho g \sin\theta h_0$.

Finally, the critical shear stress τ_c, at which the flow destabilizes (black-solid-line plotted in Fig. 2b of the main text), is obtained numerically by finding the value of τ_b for which $A(\tau_c) = 0$, i.e., $\mathcal{G}(\tau_b = \tau_c) = 3/2$. From the value of τ_c, we obtain the critical Reynolds number (black-solid-line plotted in Fig. 2(a) of the main text)

$$Re_c \equiv \frac{3u_0^2}{gh_0\sin\theta} = \frac{3\tau_c^3(\phi_J(\tau_c) - \phi)^4}{9\eta_s^2\rho g^2\sin^2\theta}[\mathcal{G}(\tau_c)]^2 = \frac{3\tau_c^3(\phi_J(\tau_c) - \phi)^4}{4\eta_s^2\rho g^2\sin^2\theta}. \tag{8}$$

References

1. Seto, R., Mari, R., Morris, J. F. & Denn, M. M. Discontinuous shear thickening of frictional hard-sphere suspensions. *Phys. Rev. Lett.* **111**, 218301 (2013).
2. Mari, R., Seto, R., Morris, J. F. & Denn, M. M. Shear thickening, frictionless and frictional rheologies in non-brownian suspensions. *J. Rheol.* **58**, 1693–1724 (2014).
3. Wyart, M. & Cates, M. E. Discontinuous shear thickening without inertia in dense non-brownian suspensions. *Phys. Rev. Lett.* **112**, 098302 (2014).
4. Guy, B. M., Hermes, M. & Poon, W. C. K. Towards a unified description of the rheology of hard-particle suspensions. *Phys. Rev. Lett.* **115**, 088304 (2015).
5. Lin, N. Y. C. et al. Hydrodynamic and contact contributions to continuous shear thickening in colloidal suspensions. *Phys. Rev. Lett.* **115**, 228304 (2015).
6. Clavaud, C., Bérut, A., Metzger, B. & Forterre, Y. Revealing the frictional transition in shear-thickening suspensions. *Proc. Natl. Acad. Sci.* **114**, 5147–5152 (2017).

7. Comtet, J. et al. Pairwise frictional profile between particles determines discontinuous shear thickening transition in non-colloidal suspensions. *Nat. Commun.* **8**, 15633 (2017).

8. Clavaud, C., Metzger, B. & Forterre, Y. The darcytron: a pressure-imposed device to probe the frictional transition in shear-thickening suspensions. *J. Rheol.* **64**, 395 (2020).

9. Pan, Z., de Cagny, H., Weber, B. & Bonn, D. S-shaped flow curves of shear thickening suspensions: direct observation of frictional rheology. *Phys. Rev. E* **92**, 032202 (2015).

10. Mari, R., Seto, R., Morris, J. F. & Denn, M. M. Nonmonotonic flow curves of shear thickening suspensions. *Phys. Rev. E* **91**, 052302 (2015).

11. Chacko, R. N., Mari, R., Cates, M. E. & Fielding, S. M. Dynamic vorticity banding in discontinuously shear thickening suspensions. *Phys. Rev. Lett.* **121**, 108003 (2018).

12. Singh, A., Mari, R., Denn, M. M. & Morris, J. F. A constitutive model for simple shear of dense frictional suspensions. *J. Rheol.* **62**, 457–468 (2018).

13. Hermes, M. et al. Unsteady flow and particle migration in dense, non-brownian suspensions. *J. Rheol.* **60**, 905–916 (2016).

14. Saint-Michel, B., Gibaud, T. & Manneville, S. Uncovering instabilities in the spatiotemporal dynamics of a shear-thickening cornstarch suspension. *Phys. Rev. X* **8**, 031006 (2018).

15. Richards, J. A., Royer, J. R., Liebchen, B., Guy, B. M. & Poon, W. C. K. Competing timescales lead to oscillations in shear-thickening suspensions. *Phys. Rev. Lett.* **123**, 038004 (2019).

16. Abdesselam, Y. et al. Rheology of plastisol formulations for coating applications. *Polym. Eng. Sci.* **57**, 982–988 (2017).

17. Blanco, E. et al. Conching chocolate is a prototypical transition from frictionally jammed solid to flowable suspension with maximal solid content. *Proc. Natl. Acad. Sci.* **116**, 10303–10308 (2019).

18. LaFarge. Superplasticizers: the wonder of fluid concrete. https://www.youtube.com/watch?v=CSZxjQwDKF038 (2013).

19. Balmforth, N. J., Bush, J. W. M. & Craster, R. V. Roll waves on flowing cornstarch suspensions. *Phys. Lett. A* **338**, 479–484 (2005).

20. Kapitza, P. L. & Kapitza, S. P. Wave flow of thin viscous fluid layers. *Zh. Eksp. Teor. Fiz.* **18**, 3–28 (1948).

21. Craster, R. & Matar, O. Dynamics and stability of thin liquid films. *Rev. Mod. Phys.* **81**, 1131 (2009).

22. Jeffreys, H. The flow of water in an inclined channel of rectangular section. *Philos. Mag.* **49**, 793–807 (1925).

23. Dressler, R. F. Mathematical solution of the problem of roll-waves in inclined opel channels. *Commun. Pure Appl. Math.* **2**, 149–194 (1949).

24. Needham, D. J. & Merkin, J. H. On roll waves down an open inclined channel. *Proc. R. Soc. Lond. A. Math. Phys. Sci.* **394**, 259–278 (1984).

25. Trowbridge, J. Instability of concentrated free surface flows. *J. Geophys. Res. Oceans* **92**, 9523–9530 (1987).

26. Liu, K. & Mei, C. C. Roll waves on a layer of a muddy fluid flowing down a gentle slope-a bingham model. *Phys. Fluids* **6**, 2577–2590 (1994).

27. Forterre, Y. & Pouliquen, O. Long-surface-wave instability in dense granular flows. *J. Fluid Mech.* **486**, 21–50 (2003).

28. Whitham, G. B. *Linear and nonlinear waves*, vol. 42 (John Wiley & Sons, 2011).

29. Benjamin, T. B. Wave formation in laminar flow down an inclined plane. *J. Fluid Mech.* **2**, 554–573 (1957).

30. Yih, C.-S. Stability of liquid flow down an inclined plane. *Phys. Fluids* **6**, 321–334 (1963).

31. Liu, J., Paul, J. D. & Gollub, J. P. Measurements of the primary instabilities of film flows. *J. Fluid Mech.* **250**, 69–101 (1993).

32. Georgantaki, A., Vatteville, J., Vlachogiannis, M. & Bontozoglou, V. Measurements of liquid film flow as a function of fluid properties and channel width: evidence for surface-tension-induced long-range transverse coherence. *Phys. Rev. E* **84**, 026325 (2011).

33. Pollak, T., Haas, A. & Aksel, N. Side wall effects on the instability of thin gravity-driven films from long-wave to short-wave instability. *Phys. Fluids* **23**, 094110 (2011).

34. Ng, C.-O. & Mei, C. C. Roll waves on a shallow layer of mud modelled as a power-law fluid. *J. Fluid Mech.* **263**, 151–184 (1994).

35. Goddard, J. Material instability in complex fluids. *Annu. Rev. Fluid Mech.* **35**, 113–133 (2003).

36. Divoux, T., Fardin, M. A., Manneville, S. & Lerouge, S. Shear banding of complex fluids. *Annu. Rev. Fluid Mech.* **48**, 81–103 (2016).

37. Sedes, O., Singh, A. & Morris, J. F. Fluctuations at the onset of discontinuous shear thickening in a suspension. *J. Rheol.* **64**, 309–319 (2020).

38. Boersma, W., Baets, P., Lavn, J. & Stein, H. Time-dependent behavior and wall slip in concentrated shear thickening dispersions. *J. Rheol.* **35**, 1093–1120 (1991).

39. von Kann, S., Snoeijer, J. H., Lohse, D. & van der Meer, D. Nonmonotonic settling of a sphere in a cornstarch suspension. *Phys. Rev. E* **84**, 060401 (2011).

40. Von Kann, S., Snoeijer, J. H. & Van Der Meer, D. Velocity oscillations and stop-go cycles: The trajectory of an object settling in a cornstarch suspension. *Phys. Rev. E* **87**, 042301 (2013).

41. Nakanishi, H. & Mitarai, N. Shear thickening oscillation in a dilatant fluid. *J. Phys. Soc. Jpn.* **80**, 033801 (2011).

42. Saint-Venant, A. J. C. Théorie du mouvement non-permanent des eaux, avec application aux crues des rivières et è l'introduction des marées dans leur lit. *C. R. Acad. Sc. Paris* **73**, 147–154 (1871).

43. Perrin, H., Clavaud, C., Wyart, M., Metzger, B. & Forterre, Y. Interparticle friction leads to nonmonotonic flow curves and hysteresis in viscous suspensions. *Phys. Rev. X* **9**, 031027 (2019).

44. Lucas, A., Mangeney, A. & Ampuero, J. P. Frictional velocity-weakening in landslides on earth and on other planetary bodies. *Nat. Commun.* **5**, 1–9 (2014).

45. Orihara, H. et al. Negative viscosity of a liquid crystal in the presence of turbulence. *Phys. Rev. E* **99**, 012701 (2019).

46. Loisy, A., Eggers, J. & Liverpool, T. B. Active suspensions have nonmonotonic flow curves and multiple mechanical equilibria. *Phys. Rev. Lett.* **121**, 018001 (2018).

47. Bain, N. & Bartolo, D. Dynamic response and hydrodynamics of polarized crowds. *Science* **363**, 46–49 (2019).

48. Charru, F., Andreotti, B. & Claudin, P. Sand ripples and dunes. *Annu. Rev. Fluid Mech.* **45**, 469–493 (2013).

49. Anderson, T. & Jackson, R. Fluid mechanical description of fluidized beds. stability of state of uniform fluidization. *Ind. Eng. Chem. Fundamentals* **7**, 12–21 (1968).

50. Lighthill, M. J. & Whitham, G. B. On kinematic waves i. flood movement in long rivers. *Proc. R. Soc. Lond. Ser. A. Math. Phys. Sci.* **229**, 281–316 (1955).

51. Lighthill, M. J. & Whitham, G. B. On kinematic waves ii. a theory of traffic flow on long crowded roads. *Proc. R. Soc. Lond. Ser. A. Math. Phys. Sci.* **229**, 317–345 (1955).

Acknowledgements

Author contributions

B.D.T., H.L., Y.F., and B.M. designed and performed experiments and analyzed the data. Y.F. developed the model. All authors discussed the results and wrote the manuscript.

Competing interests

The authors declare no competing interests.

Additional information

Supplementary information is available for this paper at https://doi.org/10.1038/s42005-020-00500-4.

Correspondence and requests for materials should be addressed to B.M.

Reprints and permission information is available at http://www.nature.com/reprints

Publisher's note Springer Nature remains neutral with regard to jurisdictional claims in published maps and institutional affiliations.